Proton-induced x-ray analysis of monazite inclusions possessing pleochroic halos

T. A. Cahill,* N. R. Fletcher, L. R. Medsker, J. W. Nelson, and H. Kaufmann

Department of Physics, Florida State University, Tallahassee, Florida 32306

R. G. Flocchini

Department of Physics and Crocker Nuclear Laboratory, University of California, Davis, California 95616

X-ray spectra were observed from proton-induced excitation of monazite inclusions possessing both normal and giant pleochroic halos at $E_p = 4.7$ and 5.7 MeV. A complete elemental analysis of these spectra is reported for elements with $Z \geq 26$. Weak photopeaks are observed from monazite inclusions possessing giant halos which are absent from inclusions with normal halos, although limitations in spatial resolution of the proton beam prevented accumulation of statistically definitive data. Because of energy, width, and intensity anomalies, some of these weak photopeaks are not readily interpretable as x rays or γ rays of known elements. Proposed evidence for superheavy elements is carefully examined.

> NUCLEAR STRUCTURE, Elemental analysis, measured proton-induced x-ray spectra from monazite inclusions with pleochroic halos, $E_p = 4.7$ and 5.7 MeV.

I. INTRODUCTION

The radioactivity from microscopic crystalline inclusions containing uranium and/or thorium etches halo regions of different optical transparency in the surrounding mica matrix. The vast majority of these halos are well understood in terms of α-particle emission from uranium, thorium, and their daughter products. Halos of larger diameter, called giant halos, are occasionally observed. These would require α energies of around 12 to 14 MeV to produce such damage although other chemical or physical processes cannot, in all cases, be discounted.[1] Certain inclusions, largely monazite (Ce, La, Th) PO_4, in biotite mica from one African deposit, possess giant halos that are not readily explained by chemical or physical models, especially since numerous normal uranium/thorium halos are exhibited by chemically similar monazite inclusions in the same mica carrier.

The analysis of x rays from monazites reported herein are based solely on data obtained prior to an earlier introduction to this work,[2] although the extent of data reported and the analysis are both greatly expanded. Attempts to observe differences in the elemental composition of normal and giant halo inclusions through particle induced x-ray emission (PIXE)[3] are described in detail. Such differences could include variations in amounts of known α emitting species, anomalous amounts of fission or α decay products from extinct α emitting species, or unknown elements that could be associated with energetic α particles as either the source of a decay chain or the radiogenic product of extinct elemental

species. Consideration is therefore required of not only normal species but also elements heavier than uranium, superheavy elements with long half-lives.

The experiment is based upon detection of characteristic x rays, as these provide in principle a definitive method of elemental analysis. The study is constrained by the small number of giant halo inclusions available, which encourages nondestructive analyses. The small mass per inclusion, typically about 1 μg, and the wide range of known and potential elemental constituents of the inclusions further constrained the measurements. Detection of superheavy elements by K x rays is not promising, since at the energies predicted[4] numerous γ transitions are known to be present from rare earths contained in monazite.[5] Excitation energies adequate to efficiently excite the K x rays could also induce severe γ-ray competition. Detection of L x rays provides an attractive method, since accurate predictions of x-ray energies and intensities, especially from the $p^{3/2}$ shell, are also available for potential superheavy constitutents and the L-vacancy production cross sections are larger by a factor $> 10^3$. The chemical nature of monazite inclusions also encourages the use of L x rays to search for the possible presence of superheavy elements, since a window is present in the spectrum between the most energetic L transitions of uranium (~ 21.5 keV) and the least energetic K transitions of the rare earths (~ 33 keV). This energy window corresponds to predictions for L_{III} shell x rays of elements from $Z = 105$ to $Z = 130$. The elements with $121 \leq Z \leq 164$ are predicted to form a superactinide series, and are thus possible candidates

for chemical bonding into a monazite crystal.

Excitation of L x rays through use of low energy electron beams, such as provided by a scanning electron microscope, while possessing excellent spatial resolution, suffers from electron bremsstrahlung background which severely limits trace element detection. Such studies of monazite inclusions have given information on major monazite constituents, while showing radial spatial concentration inhomogeneities on the scale of a few microns for elements such as uranium. Use of standard x-ray fluorescence is hampered by inadequate photon source intensity and lack of spatial resolution. Proton beams are capable of providing intense excitation of L x rays, adequate spatial resolutions, and good trace elements sensitivity.

II. EXPERIMENTAL TECHNIQUES

In the present experiment beam energies were constrained to be greater than about 4.5 MeV, in order to excite x rays deep in the inclusion, and less than 5.8 MeV, in order to avoid background from the $^{27}Al(p,n)$ reaction in the beam handling system. At an incident proton energy of 5.7 MeV, removal of electrons bound with ~35 keV from atoms at the back of an 80 μm inclusion is predicted to be reduced to about 20% of the value at the front surface, while for 4.7 MeV protons, this value is reduced to less than 10%. Thus, the analysis is most sensitive to the front third of each inclusion, and becomes quite insensitive for the rest of the inclusion.

Preparation of a well focused proton beam is essential for adequate excitation. Inclusions studied ranged in size from about 50 to 250 μm. Since the inclusions were originally analyzed in the mica matrix, focusing had to be adequate to prevent excitation of the mica, as this would reduce sensitivity to the monazite and introduce extraneous x rays primarily from rubidium, niobium, and barium. No attempt was made to obtain spatial resolution better than 50 μm and no direct measure of the beam profile was obtained.

A beam handling system adequate for these requirements was adopted from an existing target chamber[6] and slit assemblies,[7] as diagrammed in Fig. 1. Protons of 4.7 or 5.7 MeV were provided by the Florida State University tandem Van de Graaff accelerator. Two sets of slits were placed at either end of a quadrupole doublet, with the upstream slits used only for reducing beam intensity on the defining downstream slits near the target chamber. Samples were placed on target frames at an angle of 45° to the incident beam,
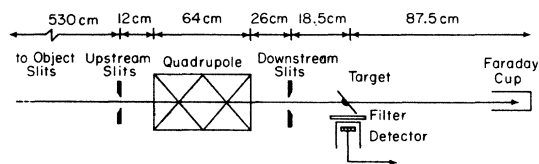
FIG. 1. Schematic diagram of beam handling system.

either open faced in their mica matrices or removed and mounted on 50 μg/cm^2 carbon backings. A Faraday cup was placed downstream for current integration, although integrations were of little use due to multiple scattering or beam stopping in the crystal. The x rays from the inclusions passed through a 0.22 μg/cm^2 aluminum absorber and were detected by an 80 mm^2 × 5 mm LN-cooled Si(Li) x-ray detector. The characteristics of the absorber were chosen in order to optimize the system efficiency at an x-ray energy near 27 keV. This reduces the intense thorium and uranium L x rays which provide most of the count rate, and thus the greatest potential for pulse pileup and gain shift effects is minimized. The x-ray detector was nominally capable of resolution of 165 eV at an x-ray energy of 5.9 keV. Pulses from the detector were processed by an on-line data acquisition computer system developed for trace element analysis projects at Florida State University. Data reduction was accomplished using computer codes developed at Flordia State[8] and Davis[9] for resolution of complex K-, L-, and M-line x-ray spectra. The x-ray detector, electronics, and data reduction codes have successfully participated in formal multielement, intermethod, and interlaboratory comparisons.[10]

When bombarding small inclusions in the original mica often after a matter of hours, rubidum x rays could appear, indicating that the beam had defocused or wandered off the inclusion and onto the surrounding mica matrix. The rate of wander is closely associated with the stability of the tandem, and some attempts to provide an adequately focused beam failed. During two run periods, one at 4.7 MeV and one at 5.7 MeV, adequate stability was achieved to allow a number of sequential analyses of a single inclusion for which data were accumulated in $\frac{1}{2}$ hour segments.

In an attempt to eliminate the effect of x rays from mica, inclusions were removed from the mica matrix and placed on 50 μg/cm^2 carbon foils with silicone grease. In this case, a sharp reduction in count rate is observed when the beam irradiates only the backing making beam stability more easily monitored, although losses of inclusions during handling and irradiation increased. The temperature of the inclusions during irradia-

tion is estimated to be below 200 °C, based on microscopic inspection of the inclusions and backings and studies of the breakdown of the silicone grease at elevated temperatures.

III. EXPERIMENTAL RESULTS

The data set generated in the runs at 4.7 and 5.7 MeV included analyses of three normal U/Th inclusions (U/Th4B, 11, and 19B) and four giant halo inclusions (GH6, 15, 19A, and 19D). Complete spectra obtained from giant halo inclusions 19A and 15, not shown in the previous work,[2] are shown in Figs. 2 and 3. Inclusions 19A, B, and D were located within a few millimeters of each other in the same mica chip but were removed to carbon backings for proton bombardment. Analyses of inclusions U/Th19B and GH19D were performed both with and without the filter, enabling elemental content to be determined for elements as light as silicon. Results of these analyses are shown in Table I for inclusion U/Th19B. Attenuation corrections for x rays from lighter elements are severe, so results for these elements must be considered approximate.

Also included in Table I are results[5] of other analyses of monazites. It can be seen that while many elements have a high variability from sam-

ple to sample, mean values are similar to results of this work for most elements, especially the absolute content of lead, uranium, and thorium. The concentrations of lead are consistent with ages between 0.6 and 0.8 billion years for all inclusions, assuming all lead is radiogenic and none has been lost.[11] Lead content in a giant halo region of the mica irradiated after removal of the inclusion, is less than 8 ppm, or at least 300 times lower than is typical in the inclusions. The thorium content in the halo region is less than 20 ppm, or at least 3000 times lower than in a typical inclusion. The high iron value seen in these monazites may reflect the iron rich biotite mica matrix, although the iron is in the monazite itself.

During a period of high beam stability at 5.7 MeV, a number of analyses were performed on the following inclusions: U/Th11 (1 analysis), GH15 (6 analyses), GH19D (8 analyses), U/Th19B (4 analyses), and GH19A (14 analyses). Mean values of elemental content were calculated relative to those of U/Th19B with the relative thorium concentration normalized to unity. These values are shown in Table II. Standard deviations in the results of successive analyses are given, calculated as the quadratic sum of the U/Th19B variance and that observed in each inclusion. Systematic enrichment of light rare earths and uranium are seen in giant halo inclusions although they are not significantly outside the range of values reported for other monazites cited in Table I and Ref. 5. The enrichment shown in lead is of doubtful significance, due to the importance of x-ray attentuation effects, but it is in accord with the slight increase in uranium content.

Repeated analyses show small variations in major
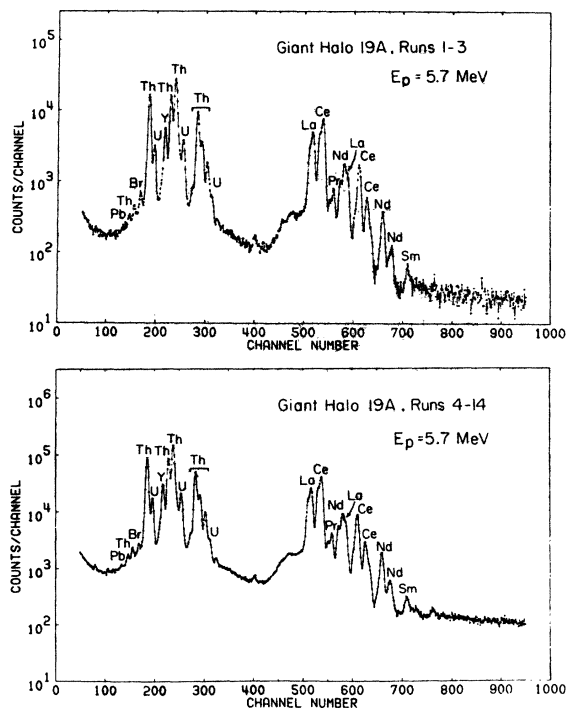
FIG. 2. X-ray spectra from 5.7 MeV proton bombardment of inclusion GH19A. Changes in relative intensities of the bromine line and the line near channel 400 are discussed in the text.
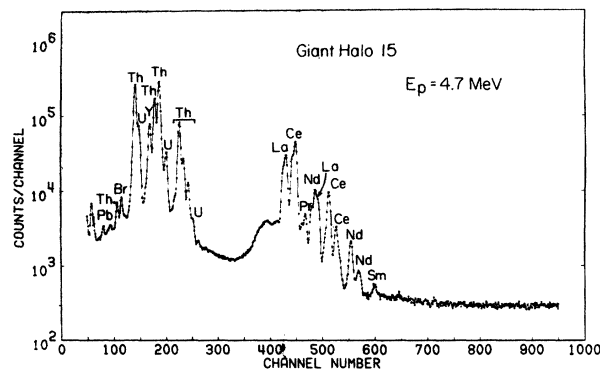
FIG. 3. X-ray spectrum from 4.7 MeV proton bombardment of inclusion GH15. The energy calibration (keV/channel) is different in Figs. 2 and 3. The relative decrease in lanthanide x rays is due to the relatively lower K-shell vacancy production cross section at $E_p = 4.7$ MeV.

TABLE I. Mass percent elemental content in monazites.

Element	Present work inclusion U/Th 19B (%)	Mean (%)	Other monazites [a] (No. analyses)	Min. (%)	Max. (%)
O	26 [b]	24	(9)	...	...
P	~12	12	(9)	11.6	12.8
Sc [c]	~0.2	...	...	...	...
Y	0.35	3.7	(3)	3.4	4.0
La	11	27	(7)	16.8	32.9
Ce	20	22	(7)	12.1	30.9
Pr	1.6	2.5	(1)	...	...
Nd	5.6	7	(1)	...	...
Sm	0.9	0.7	(1)	...	...
Gd	0.8	...	...	...	...
Th	6.7	8.1	(9)	0.0	27.7
U	0.84	1.0	(5)	0.2	3.4
Pb	0.24	0.26	(6)	0.1	0.9
H	...	0.04	(6)	0.007	0.10
Si	~0.3 [d]	0.8	(9)	0.1	1.3
K	~0.4	...	...	...	...
Ca	~0.2	1.0	(7)	0.0	4.5
Fe	13.5	0.9	(7)	0.0	2.0

[a] See Ref. 5.
[b] Estimated stochiometrically.
[c] Elements scandium through uranium as listed are in chemical subgroup 3b, preferred for binding in monazite.
[d] Silicone adhesive was used to fix this inclusion to a carbon backing.

elemental constituents of inclusions, thus providing evidence for the reliability of the analysis system, including the automatic data reduction codes. They also provide evidence of the energy stability of the analysis system, as numerous x-ray lines of known energy and high statistical significance occur in every spectrum. The values for all measurements of the x-ray energy of the Th $L\beta_1$ transition in the largest set of analyses at $E_p = 5.7$ MeV gives a standard deviation of ± 3.6 eV.

In addition to the elements listed in Tables I and II, a number were observed in trace amounts in the central low background portion of the spectra (see Figs. 2 and 3) between 22 and 29 keV. Weak photon peaks observed in that energy range, which possess unambiguous association with known element x rays, have measured energies which agree with accepted values to within an average of 13 ± 10 eV. The evidence contained in the peak width is also valuable, since it provides a way to determine whether an observed peak is a singlet x or γ ray, or is a doublet due to one of the seven elements (Ag, Cd, In, Sn, Sb, Te, and I) whose $K\alpha_{1,2}$ doublet x rays fall in this energy region. The width (and shape) of the partially resolved $K\alpha_{1,2}$ transitions of these elements sets them apart

from singlet transitions as shown in Fig. 4. At 26.3 keV, for example, one could have either a Sb $K\overline{\alpha}$ transition with a width of 480 ± 15 eV or a singlet transition with a width of 345 ± 10 eV. Unambiguously identified peaks in the energy region 22 to 29 keV have measured widths which agree with those expected for the resolution of the detection system to within 20 ± 20 eV.

The evidence contained in secondary x-ray transitions is also important, since any tentative identification of weak lines will include predictions of other transitions. The ratios of L transitions in actinides induced by ion beams have been measured at these ion velocities, and they closely match predictions of relativistic Hartree-Fock-Slater calculations.[12] Likewise, ratios of K transitions are well known and they have been remeasured using many single elements standards as part of this work. Their greatest value to this work lies in associating a weak line that could be a $K\beta_1$ or $K\beta_2$ transition of an element from rhodium through iodine, with a stronger $K\alpha_{1,2}$ transition. The absence of the stronger transition would eliminate that particular elemental association.

There is a potential problem of unknown γ rays and x rays in this spectral region (22 to 29 keV), since the elemental composition of the inclusion

TABLE II. Elemental composition of inclusions relative to U/Th19B (see Table I for absolute values for U/Th19B), normalized to thorium, and determined at $E_p = 5.7$ MeV.

Element	U/Th11	GH15	GH19A	GH19D
Y	1.00 ± 0.01 ...	1.10 ± 0.01 (± 0.05) [a]	1.14 ± 0.02 (± 0.02)	1.37 ± 0.01 (± 0.01)
La	1.17 ± 0.01 ...	1.25 ± 0.01 (± 0.02)	1.25 ± 0.01 (± 0.04)	1.22 ± 0.01 (± 0.01)
Ce	1.11 ± 0.01 ...	1.25 ± 0.01 (± 0.02)	1.25 ± 0.01 (± 0.02)	1.23 ± 0.01 (± 0.01)
Pr	0.74 ± 0.03 ...	1.28 ± 0.03 (± 0.08)	1.27 ± 0.04 (± 0.09)	1.29 ± 0.03 (± 0.06)
Nd	1.09 ± 0.01 ...	1.27 ± 0.01 (± 0.04)	1.34 ± 0.02 (± 0.10)	1.30 ± 0.02 (± 0.04)
Sm	1.6 ± 0.20 ...	1.59 ± 0.3 (± 0.32)	2.2 ± 0.3 (± 1.0)	1.84 ± 0.25 (± 0.44)
Gd	N.D. [b] ...	1.93 ± 0.3 (± 0.26)	1.5 ± 0.4 (± 0.9)	1.85 ± 0.3 (± 0.32)
U	0.90 ± 0.01 ...	1.05 ± 0.01 (± 0.04)	1.17 ± 0.02 (± 0.02)	1.10 ± 0.01 (± 0.01)
Br	~3.3	~6.7	42 ± 5	~1.9
Pb	1.06 ± 0.2 ...	1.36 ± 0.2 (± 0.2)	1.02 ± 0.5 (± 0.3)	1.33 ± 0.25 (± 0.13)

[a] Values in parentheses represent one standard deviation in the ratio as calculated from repeated analyses.

[b] N.D. denotes not determined.

is known to be rich in rare earths and actinides. The use of uranium-thorium halo inclusion and giant halo inclusion comparisons was designed to cover these possibilities, since their compositions, though complicated, are similar, as subsequently proven in Table II, and therefore they should possess similar x-ray and γ-ray structure. Each set of data includes both normal halo and giant halo inclusions, and the spectra were compared for differences that might be associated with the different types of halos.

In a continuation of this work, a search was made by Fox et al.[13] for all γ rays in the 10 to 100 keV region, utilizing targets of normal isotopic abundance for every nonradioactive, non-noble gas element with $Z \geqslant 9$. Several new γ rays were found including one at 27.23 ± 0.03 keV, from the reaction $^{140}Ce(p, n\gamma)^{140}Pr$. Since the threshold for the reaction is at 4.2 MeV, and since ^{140}Ce represents 88.5% of normal cerium, this γ ray produces small though important contributions to the spectra. The intensities of the γ ray reported herein and originally by Fox et al.[13] are in agreement with an independent evaluation after detector efficiency corrections are considered.[14]
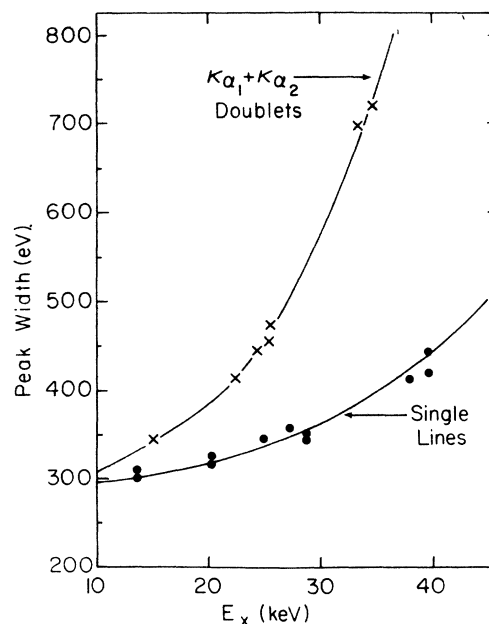
FIG. 4. Measured peak widths versus photon energy for singlet x or γ rays and doublet $K\alpha_1 + K\alpha_2$ x rays. The solid line through the doublet values is an approximate convolution of the singlet widths, $K\alpha_1/K\alpha_2$ intensity ratios, and energy separations.
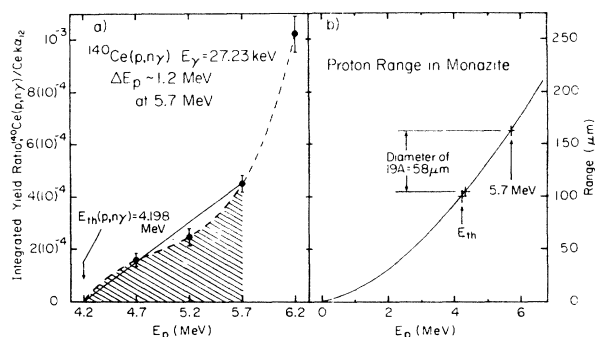
FIG. 5. Measured integrated yield ratio of the 27.23 keV γ ray from ^{140}Ce $(p,n\gamma)$ relative to the integrated Ce $K\alpha_{1,2}$ x-ray yield for a target thickness of ~1.2 MeV at $E_p = 5.7$ MeV. The range curve for protons in monazite shows the energy thickness of GH19A to be ~1.4 MeV.

The intensity of this γ ray relative to the integrated intensity of the Ce $K\alpha_{1,2}$ x rays has been measured using the identical detector and filter system used for all of the monazite spectra. This yield ratio is shown vs proton energy in Fig. 5. The CeO$_2$ target thickness resulted in a proton energy loss of ~1.2 MeV at $E_p = 5.7$ MeV, which corresponds to the average energy loss in a uniformly illuminated monazite inclusion of ~75 μm in diameter (average thickness = $\frac{2}{3}$ diameter). The ratio at $E_p = 5.7$ MeV from a monazite inclusion will be lower than that shown in Fig. 5 by up to a factor of 2 for the larger inclusions. From the data of Fig. 5, expected ratios are calculated for the inclusion sizes and proton energies used in this study and predicted contributions from the ^{140}Ce$(p,n\gamma)$ reaction are made knowing the Ce $K\alpha_{1,2}$ intensity for each spectrum. The elemental content, measured relative to the thorium content, is found to be nearly constant for several runs on a particular inclusion for the primary monazite constituents, those which presumably are chemically bound in the crystal. Other relatively weak x rays show large and systematic variations from analysis to analysis. The largest set of sequential analyses was obtained for inclusion GH19A at 5.7 MeV. The 14 sequential runs for GH19A had peak to background ratios for a number of weak lines which were adequate for individual analysis. The measured concentrations of Y, Ce, and U relative to Th and normalized to the first run are shown in the upper portion of Fig. 6 to be constant within a few percent (see also Table II). Unlike these primary monazite elements, the concentration of bromine and the yield for photon lines at ~26.3 and 27.3 keV show correlated variations. In addition to these three spectral components, indium was
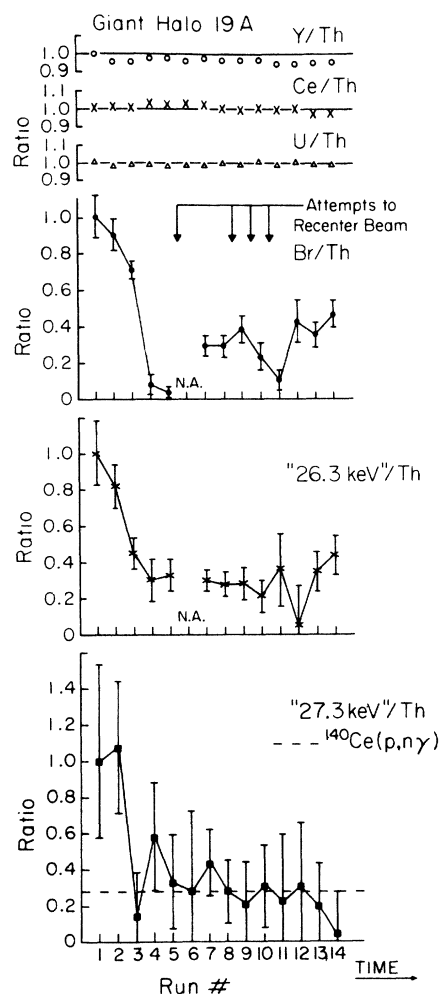
FIG. 6. Elemental concentrations relative to thorium normalized to the first of 14 sequential analysis runs on giant halo inclusion 19A at $E_p = 5.7$ MeV. Values for yttrium, cerium, and uranium, components of monazite, are nearly constant while the yields from bromine and the lines at ~26.3 and ~27.3 keV are not. Attempts to recover the initial spectrum by refocusing the beam on the inclusion are indicated after runs Nos. 5, 8, 9, and 10.

also found to be present in small amounts during the first three runs but absent thereafter. The sixth run in the sequence was of such short duration that no analysis for weak spectral lines could be made.

Attempts were made to recover the initial spectra which showed these trace contributions more strongly. Prior to runs numbered 6, 9, 10, and 11 the beam was reconstituted by maximizing total count rate and resetting the slits. These recovery attempts are indicated in Fig. 6, which also show their lack of success.

The nature of the peak seen near 26.3 keV
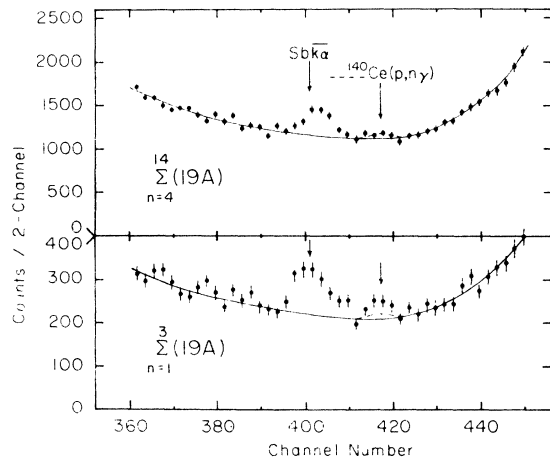
FIG. 7. Spectra from giant halo inclusion 19A for the
first three analyses and all other analyses. The
background shape is unchanged in the two spectra.
Calculated yields of the γ ray at 27.23 keV from the
^{140}Ce $(p,n\gamma)$ reaction are indicated in both spectra.
Arrows show expected positions of the Sb $K\overline{\alpha}$ x ray and
the γ ray. There are significant changes in the energy
and width of the 26.3 keV line (near channel No. 400)
and in the yield at the 27.3 keV line (near channel No. 418).

changed significantly during the course of the 14
sequential runs on inclusion GH19A as shown in
Fig. 7. For the sum of the first three analyses the
central energy of the peak was 26 219 ± 20 eV, while
the peak width was 525 ± 30 eV. The sum of the re-
maining analyses (upper portion of Fig. 8) indicated
an energy of 26 337 ± 15 eV and a width of 376 ± 43 eV.
The individual analyses had even larger width range
than these sum spectra, from 600 ± 50 eV for run 1 to
330 ± 30 eV for run 14. The transition in energy
and probably width occurs between the third and fourth
analyses and shows little variation for the re-
maining analyses. This change does not appear
to be an artifact of the analytical system, since
no other statistically sound peak shows such be-
havior in either energy or width. Peaks with sta-
tistical strength similar to the 26.3 keV line
(Th L_l, U $L\gamma_4$, Sm $K\beta_1$, see Figs. 2 and 3), when
treated in the same manner, show no change in
amount to within ± 15%, in energy to within ~ 15 eV,
or in width to within ~ 30 eV. The changes in the
26.3 keV line are significant and the data following
analysis No. 3 favors a singlet interpretation.

The second most extensive set of sequential
analyses occurred for the nine sequential runs
of giant halo inclusion GH15 at E_p = 4.7 MeV.
Figure 8 shows some elemental content ratios
similar to Fig. 6. Major monazite constituents
are observed to undergo ~ 15% variations relative
to thorium, whereas a spectral contribution near
27.26 keV shown relative to that of the seventh
analysis, which represents 16% of all data on this
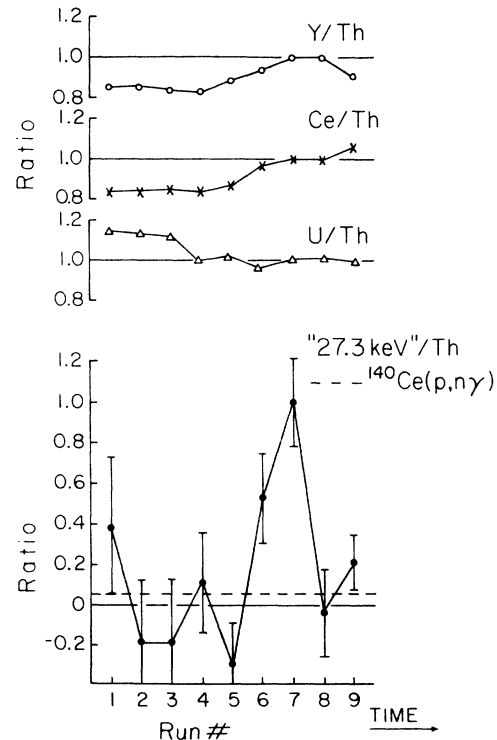
FIG. 8. Elemental concentration relative to thorium
and normalized to the seventh of nine sequential analysis
runs on giant halo inclusion 15 at E_p = 4.7 MeV. The
yield of the 27.3 keV line shows significant fluctuation.

inclusion, shows a sudden increase at the seventh
analysis followed by an equally sudden extinction
in the eighth and ninth analyses. Figure 9 shows
the 25 to 29 keV portions of the spectra from the
seventh run on GH15 and from the sum of all re-
maining runs. The spectra are plotted on different
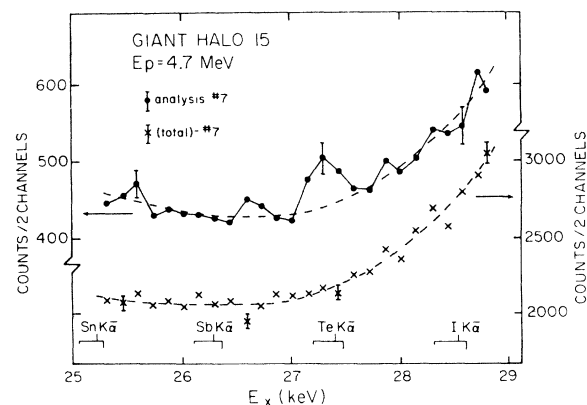
FIG. 9. Spectra from giant halo inclusion 15 at E_p = 4.7
MeV. Results of the seventh analysis (scale on left) are
compared with the sum of all other analyses (scale on
right). Self-consistent backgrounds for minimum χ^2
are shown in both cases, including the peak at 27.25 keV.

scales with different suppressed zeros. The width of the 27.26 keV peak observed in run 7 is 360 ± 30 eV, consistent with that expected for a singlet x ray or a γ ray. The expected photon yield from the $^{140}Ce(p,n\gamma)$ reaction is only ~5% of that observed in run 7 (see Fig. 8) due partly to the nearness to threshold but more importantly due to the large size of the GH15 crystal (~124 μm diam).

Possible causes of the intensity variations observed include vaporization of the source of the spectral line and a spatially inhomogeneous elemental distribution in the inclusions accompanied by beam spot wandering or defocusing. No direct measure of beam size or position was made. The intensity results for bromine and the 26.3 keV line (Fig. 6) are consistent with vaporization whereas the behavior of the of the 27.26 keV intensity is not (see Fig. 8). Volatilization of trace elements would locate them preferentially near the crystal surface which would be consistent for any impurities in compound form or with any valence inappropriate for bonding in the monazite. Thus, volatility and inhomogeneity may be closely linked. Whatever the cause of such variability it is likely that some information is lost by simple summation of all data when yield ratios are changing. Thus

each spectrum had to be treated individually although summing was used when all indications pointed to similar behavior or when it was statistically necessary.

Data on all statistically significant photon lines observed in the energy range 22 to 29 keV are listed in Table III. The standard criterion of significance, intensity greater than three standard deviations from background, was used. Peaks were fitted by Gaussian functions unconstrained in width, height, and location. Data on each peak include energy (E), uncertainty in energy (ΔE), full width at half maximum (W), width uncertainty (ΔW), the number of counts in each peak (N), with statistical uncertainty (ΔN_s), and uncertainty in background estimate (ΔN_b). The width error is an estimate from different methods of evaluating width, since the computer produced width errors which were unreasonably small. Backgrounds were derived from self-consistent least squares fits to regions of the spectra in which peak structure was absent. Since major sources of the background, Compton events and bremsstrahlung in the inclusion, are known to lack structure, fits were constrained to minimum curvature for reasonable χ^2. In several cases, inclusions similar in size and composition aided in establishing

TABLE III. Data on all photon peaks (data are from the total of all runs on a particular inclusion at the proton energy specified unless otherwise indicated) between 22 and 29 keV.

E_p (MeV)	Inclusion	$(E \pm \Delta E)$ (eV)	$(W \pm \Delta W)$ (eV)	$(N_x \pm \Delta N_s \pm \Delta N_b)$ (counts)	Element identification
5.7	U/Th4B	None			
5.7	GH6	$27\,295 \pm 40$	250 ± 100	$224 \pm 78 \pm 60$	
4.7	U/Th4B	None			
4.7	GH6	None			
4.7	U/Th11	None			
4.7	GH15	None			
		$27\,227 \pm 30$ [a]	360 ± 30	$168 \pm 44 \pm 20$	
5.7	U/Th11	None			
5.7	GH15	$22\,108 \pm 20$	419 ± 20	$25\,302 \pm 446 \pm 200$	Ag $K\alpha_{1,2}$
		$24\,953 \pm 30$	380 ± 20	$5\,611 \pm 287 \pm 200$	Ag $K\beta_1$
		$25\,478 \pm 60$		$850 \pm 100 \pm 150$	Ag $K\beta_2$
		$27\,298 \pm 40$	305 ± 70	$305 \pm 78 \pm 50$	
5.7	GH19D	$22\,773 \pm 40$	340 ± 50	$573 \pm 138^{+345}_{-114}$	
		$25\,210 \pm 50$	495 ± 30	$246 \pm 99 \pm 60$	Sn $K\alpha_{1,2}$
		$26\,261 \pm 50$	370 ± 80	$256 \pm 92 \pm 60$	
		$27\,266 \pm 30$	370 ± 50	$708 \pm 100 \pm 60$	
		$27\,733 \pm 40$	340 ± 50	$305 \pm 70 \pm 60$	
5.7	U/TH19B	None			
5.7	GH19A	$26\,332 \pm 30$	472 ± 30	$1\,502 \pm 110 \pm 140$	
		$27\,211 \pm 60$ [b]	433 ± 65	$349 \pm 75 \pm 80$	
		$24\,159 \pm 40$ [b]	430 ± 50	$83 \pm 27 \pm 20$	In $K\alpha_{1,2}$
		$26\,219 \pm 30$ [b]	525 ± 30	$435 \pm 45 \pm 60$	
		$27\,219 \pm 30$	415 ± 50	$111 \pm 31 \pm 25$	

[a] Data from run No. 7, representing 16% of the total.
[b] Data from the sum of runs Nos. 1, 2, and 3, representing 16% of the total.

background shapes,[15] while in other cases, sequential runs on the same crystal provided information on the background.

IV. DISCUSSION OF WEAK TRANSITIONS

The information on weak transitions included in Table III, together with knowledge of sizes of the inclusions and gross elements structure, can be used to interpret these results in terms of possible elemental sources. The photons at 22.11, 24.16, and 25.21 keV are unambiguously associated with the $K\overline{\alpha}$ x rays from known elements Ag, In, and Sn, to within 20 eV in energy and width. The strong singlet line at 24.97 is identified as the Ag $K\beta_1$ x ray with the appropriate intensity for the accompanying $K\overline{\alpha}$ x ray. It is interesting to note that these two x-ray transitions in silver were observed strongly in GH15 at 5.7 MeV and not in the 4.7 MeV bombardment of GH15. The lower energy spectra where silver lines were absent were obtained first while the exposed inclusion was still held in the original mica. Prior to the 5.7 MeV bombardment, the crystal was extracted from the mica and placed on a thin carbon backing so the crystal orientation was not preserved. The proton range curve of Fig. 5 illustrates that since GH15 had a diameter of approximately 124 μm, no appreciable x-ray yield could occur from the backside of the inclusion at E_p =4.7 MeV, thus providing a plausible explanation for the absence of silver lines in the first measurement at 4.7 MeV. Silver contamination of GH15 during transfer from the mica carrier to the carbon foil cannot be absolutely ruled out, however, no such change was observed for any other of the several inclusions investigated.

The remaining spectral lines of Table III at E_x $\simeq$22.77, 26.27, 27.26, and 27.73 keV have all been mentioned[2] as possibly involving $L\alpha_1$ transitions in superheavy elements with Z =116, 124, 126, and 127, respectively, and are treated individually in the following discussion.

The spectral line at 22 773 ± 40 eV, only observed in GH19D, has width (~340 ± 50 eV) similar to that of a singlet and its energy is close to the known $K\beta_1$ transition in rhodium (22 724 eV) and a proposed $L\alpha_1$ transition (22 712 ± 50 eV) in element Z =116. Normally the expected intensity of Th $K\overline{\alpha}$ relative to the $K\beta_1$ intensity would definitely allow or reject the presence of rhodium. The extracted yield of Rh $K\overline{\alpha}$ is near null and a factor of 20 ± 8 below that expected; however, in this case the highly sloping background in the region of 22.8 keV renders the yield of the 22.77 keV line almost useless for intensity comparison purposes.

The transition near 26.3 keV is observed in two

inclusions and it would appear to be the $K\overline{\alpha}$ line from antimony. The correlation in intensity (Fig. 6) between the Br $K\overline{\alpha}$ and the 26.3 keV line is consistent with an assumed surface contaminant of $SbBr_3$ (boiling point, 280°C) or similar compound which is slowly vaporized during bombardment. The absolute bromine content is not accurately evaluated because of the extreme effect of the filter at such a low x-ray energy. The measurements from GH19A of energy and width of the 26.3 keV line are, however, inconsistent with the $SbBr_3$ assumption. As discussed in the last section, the 26.3 keV line undergoes a systematic shift to higher energy and narrower width as the intensity decreases vs time. The display of this narrowed line shown previously[2] is the sum of runs 11 through 14 and it shows a singlet width (330 ± 30 eV). The sum of runs 4 through 14, which shows a peak energy above the Sb $K\alpha_{1,2}$ position by + 63 ± 25 eV and a width decrease by −104 ± 45 eV, is plotted in Fig. 10(a) as a difference spectrum. The background used to generate the difference spectrum is that shown in Fig. 7. The
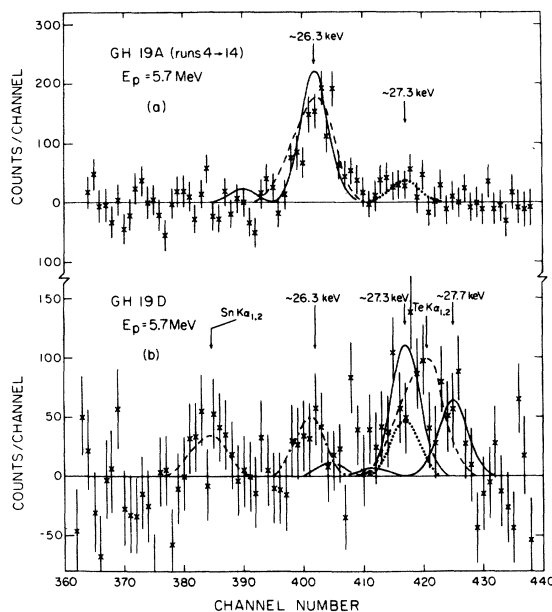
FIG. 10. Difference spectra from GH19A (Nos. 4 through 14) and GH19D obtained at E_p = 5.7 MeV. The dashed curves are fitted yields of $K\alpha_{1,2}$ doublet line shapes of known elements. The dotted curves are the calculated γ-ray yield from ^{140}Ce $(p,n\gamma)$ at 27.23 keV. The solid curves show the calculated positions and yield fitted to minimize χ^2 of $L\alpha_1$ and $L\alpha_2$ transitions for Z =124 [shown in (a)] and Z =126, 127 [shown in (b)]. The dot-dash curve is a fitted Gaussian curve yielding a width near that expected for a singlet. The subtracted background is that of Fig. 7 for part (a), for part (b) see text and Ref. 15. A best fit to the 26.3 keV line in (a) is a singlet at energy slightly higher than the $L\alpha_1$ curve shown.

curves are fixed in energy position and shape by the known energies of the 124 $L\alpha_1$, 124 $L\alpha_2$, and Sb $K\alpha_{1,2}$ transitions. Minimum values of χ^2/pt $\simeq 2$ for either assumption are obtained by varying the transition intensity. No preference can be argued therefore for the presence of $Z = 124$ from this spectrum and no unique assignment of this peak is made because of the unusual behavior of its energy and width. A singlet assignment is preferred at a slightly higher photon energy when the photon energy is a free parameter in the fitting procedure.

The spectral line near 27.3 keV is particularly interesting for a variety of reasons. It has been observed in all giant halo inclusions investigated (Nos. 6, 15, 19A, and 19D) with somewhat differring mean intensities. The mean energy and width from these observations is $27\,260 \pm 30$ and 380 ± 30 eV, respectively. The consistently small width measurements clearly indicate a singlet transition. The $K\beta_1$ transition of indium $(E_x =27\,274$ eV) can be rejected as a source of this line due to the absence of or insufficient strength in the In $K\alpha_{1,2}$ transitions at the expected location. In view of the calibration accuracies cited and the width consistency this cannot be Te $K\bar{\alpha}$ which should have $E_x = 27\,380$ eV and $\Gamma = 500 \pm 10$ eV.

The remaining known candidate is the γ-ray transition from the ^{140}Ce$(p,n\gamma)$ reaction at $E_\gamma =27\,230 \pm 30$ eV. The observed intensity variations of the 27.3 keV line (see Figs. 6 and 8) are not consistent with a γ-ray assignment. The inconsistency of the yield at 27.3 keV with the calculated yield of the γ ray is further illustrated by spectrum fits in Figs. 10 and 11. For inclusion GH19A the yield is equivalent to that expected of the γ ray [see Fig. 10(a)] although for the early runs on GH19A such is not the case (see Figs. 6 and 7). Figure 11 shows spectrum seven from GH15 at $E_p = 4.7$ MeV. Both the expected γ-ray yield and the tellurium line (shape and position) are clearly inconsistent with the observed spectrum. The χ^2 values yield confidence levels which favor the singlet by 5 to 1. The calculated γ-ray yield from ^{140}Ce$(p, n\gamma)$ as shown in Fig. 11 is very small because of the low bombarding energy and the large inclusion size. The background used is that shown in Fig. 9.

The lines observed in this energy region from inclusion GH19D are very weak and they are shown in a difference spectrum in Fig 10(b). The line near channel No. 385 is identified as Sn $K\bar{\alpha}$. The 26.3 keV line is shown fitted by a Gaussian curve with width ~370 eV, and although it appears much narrower than an Sb $K\alpha_{1,2}$ doublet, the poor statistics do not allow a definitive singlet assignment. A number of line shapes are illustrated in
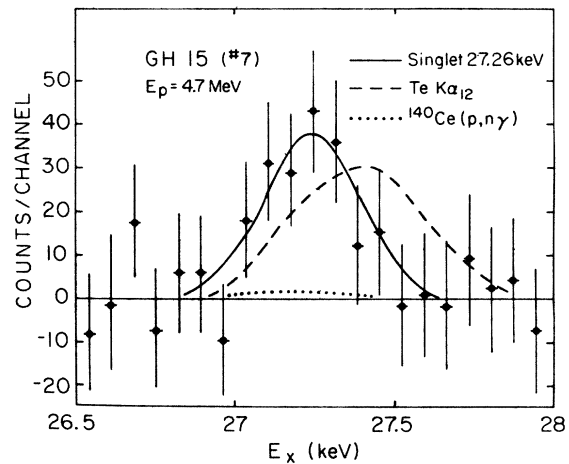
FIG. 11. Difference spectrum from GH15 (No. 7) obtained at $E_p = 4.7$ MeV. The calculated yield of the γ ray is due to the lower bombarding energy and the fact that GH15 is a large crystal. The subtracted background is that of Fig. 9.

the channel 410 to 430 region representing various possible interpretations. The solid lines are $L\alpha_1$ and $L\alpha_2$ line shapes at positions for $Z = 126$ and 127 and in amounts which minimize χ^2. The dashed line is the tellurium line shape for minimum χ^2. The dotted curve is the calculated γ-ray yield. The description of the data in this region as two singlets near 27.3 and 27.7 keV is clearly superior although not compelling. From a normalized χ^2 $\simeq 1.32$, the calculated confidence level for a two singlet interpretation, although only 13%, is favored by 5 to 1 over a tellurium assignment and by 3 to 1 over tellurium plus the calculated γ-ray yield.

The background used to generate the difference spectrum of Fig. 10(b) has been discussed in detail.[15] This background is considerably higher than that originally displayed[2] and also considerably greater than that yielding the best χ^2 from computer fitting. The best mathematical background is ~15 to 20 counts lower than the one in Fig. 10(b) and therefore fits better in the "open regions" on either side of the Sn $K\alpha_{1,2}$ line and above the 27.7 keV line. The background used in Fig. 10(b) actually minimizes the magnitude of these weak spectral lines.

The data of Table IV together with that of Fig. 5 can be used to evaluate the contribution of the ^{140}Ce$(p,n\gamma)$ yield. The value N_γ(calc) listed in Table IV is the yield calculated to fall within 1 full width at half maximum (FWHM) (not integrated yield of Fig. 5) based on these data and an assumed effective average target thickness of 74% of the inclusion diameter. The observed yield within 1 FWHM, N_x, at 27.26 keV, is extracted in

TABLE IV. Comparison of calculated ^{140}Ce($p,n\gamma$) yield to observed yield near 27.3 keV.

E_p (MeV)	Inclusion	Diameter	Ce $K\bar{\alpha}$ yield (10^3 counts)	$N \pm \Delta N_s \pm \Delta N_b$ (counts near 27.3 keV in 1 FWHM)	N_γ (calc) (counts in 1 FWHM)	$(N - N_\gamma)/\sigma_T$ [a]
5.7	U/Th4B	83 μm	74	$39 \pm 53 \pm 15$	21 ± 3	$+0.3$
5.7	GH6	100 μm	149	$184 \pm 69 \pm 40$	36 ± 5	$+1.9$
4.7	U/Th4B	83 m	253	$-10 \pm 75 \pm 40$	25 ± 6	-0.4
4.7	GH6	100 m	1784	$219 \pm 155 \pm 150$	176 ± 44	$+0.2$
4.7	U/Th11	250 m	434	$70 \pm 57 \pm 60$	43 ± 11	$+0.3$
4.7	GH15	124 m	372	$94 \pm 81 \pm 50$	37 ± 9	$+0.6$
				$154 \pm 35 \pm 15$ [b]	7 ± 2	$+3.8$
5.7	U/Th11	250 μm	247	$44 \pm 36 \pm 25$	55 ± 8	-0.25
5.7	GH15	124 μm	912	$296 \pm 82 \pm 40$	201 ± 30	$+1.0$
5.7	GH19D	60 μm	609	$534 \pm 70 \pm 50$	240 ± 24	$+3.3$
5.7	U/Th19B	124 μm	858	$91 \pm 71 \pm 25$	189 ± 28	-1.2
5.7	GH19A	58 μm	487	$323 \pm 75 \pm 53$	213 ± 41	$+1.1$
				$93 \pm 28 \pm 20$ [b]	21 ± 4	$+2.1$

Mean value of $(N - N_\gamma)/\sigma_T$:	Normal halos -0.25
	Giant halos $+1.35$
χ^2/pt. for describing 27.3 keV yield	Normal halos 0.37
as the calculated γ-ray yield:	Giant halos 2.85

[a] This ratio is the excess yield near 27.3 keV over the calculated ^{140}Ce($p,n\gamma$) yield, in units of total error.

[b] These two runs are No. 7 for GH15 and the sum of Nos. 1 and 2 for GH19A. All other values represent the total data on the inclusion without selection. Only total unselected data are used in forming net comparisons of normal halos and giant halos in the lower portion of the table.

a consistent manner from all spectra. The differences in N_x and N_γ, listed in the last column, are expressed in units of the total error σ_T, calculated as a root quadratic sum. Thus, a value less than unity implies that the difference is less than the total error. A maximum value of this normalized excess was 3.8, found for spectrum 7 from GH15 bombarded at $E_p = 4.7$ MeV, see Fig. 9.

Giant halo inclusions and uranium/thorium inclusions are compared in the lower portion of Table IV. The data demonstrate that average values of the normalized excess are near null for U/Th inclusions and in excess of unity for GH inclusions. The excess is expressed more dramatically by noting that the χ^2/pt. for describing the 27.26 keV line as the γ ray is 0.37 for the total of all U/Th inclusion spectra and 2.85 for all GH inclusion spectra. This χ^2 value yields a very high confidence level (85%) for assigning the line in U/Th inclusion spectra to the γ ray; such is not the case for GH inclusions.

An estimate of the amount of material which would be adequate to produce any certain weak spectral line must be accompanied by an assumption regarding the spatial homogeneity of the material and the beam spot size. Thus for a fractional mass of 10 ppm (parts per million) for a

line in a spectrum taken on a 1 μg crystal, the mass present would be 10 pg if the entire crystal is uniformly excited. On the other hand, if a crystal this size is irradiated uniformly with protons at 5 to 6 MeV only the front 30% is excited at high efficiency so the amount of material actually detected would be 3 pg and that amount of material located in the front 30% would yield the same spectral line as 10 pg uniformly distributed. If the material is localized at a position of efficient excitation by a proton beam spot smaller than the crystal the same fractional mass measurement could result from mass content considerably less than these figures. The actual amount of material detected is no more than 30% of the uniform distribution mass value and lower limits may be much less. Of course an upper limit may also be much greater than the uniform distribution mass value.

The amount of a potential superheavy element constituent, such as $Z = 126$, $A = 354$, can be calculated using the yield ratio with an element such as uranium, since cross sections for x-ray production from the $p_{3/2}$ electron shell vary smoothly with atomic number. This procedure yields fractional mass values from the weak spectral lines at 27.3 keV which typically range from 6 ppm (GH6, 4.7 MeV) to 45 ppm (GH19D, 5.7 MeV). The γ-ray

yield (see Table IV), within error, accounts for all the line in GH6 at 4.7 MeV but only about 40% of that from GH19D at 5.7 MeV. The remainder yields a uniform distribution fractional mass of 27 ± 6 ppm of element $Z = 126$, or ~14 pg and 2.3 $\times 10^9$ atoms, and the lower limit could be considerably less. The equivalent value for the null result in GH6 at 4.7 MeV is less than 10^{-13} g or 1.8×10^8 atoms within the irradiated volume.

The very weak Sn $K\bar{\alpha}$ line from GH19D [see Fig. 10(b)] can be analyzed in a similar fashion. Its intensity yields 14 ± 6 ppm and 7 pg or 3.6×10^{10} atoms of Sn for the uniform distribution assumption. Actual amount detected is ~$\frac{1}{3}$ of these values and other measurements[15] on this crystal may provide an appropriate bulk value which could indicate indirectly the localization observed. The tin line in the present experiment is not instrumental as noted by its complete absence in all other spectra, many of which have greater statistical significance.

V. SUMMARY

The use of particle-induced x-ray emission has been shown to provide an elemental analysis method for microscopic single crystals for all elements silicon and heavier, including possible superheavy elements. Sensitivities of a few parts per million by mass are achieved in analyses of monazite inclusions, resulting in mass sensitivities in the picogram range. The accuracy of the method is exemplified in that for GH19A 14 sequential analyses of the uranium/thorium ratio has shown a mean deviation of less than 0.2%. The lead/uranium/thorium mass ratios for all monazite inclusions studied show radiogenic ages in the range 7 ± 1 $\times 10^8$ yr. The analyses of some weak transitions indicate complicated behavior in the inclusions, due to a possible combination of spatial inhomogeneity, volatility, or other effects that exceeded the capabilities of the system, resulting in an inability to reproduce some trace element concentrations.

The earlier work[2] has lead to a number of investigations. New theoretical calculations[17] continue to show that there is considerable uncertainty in stability estimates. Some of these suggest that nuclei with $Z = 124$ and 126 might be much more

stable than previously believed. Other works suggest that nuclide formation by the r process[18] may be possible to the neighborhood of $A = 350$. A plausible explanation of giant halo formation from α particles due to ternary fission follows from predictions of unusually high ternary fission rates of some superheavy species.[19] An alternative explanation of giant halo formation, in terms of proton recoils from radiogenic α-particle scattering, has been openly discussed for some time by Middleton and others, and recently a calculation of the effect has been published.[20] Hydrogen content, necessary for such a process, is cited herein for some monazite samples (Table I) to be extremely small, although no relative measurement in normal and giant halo inclusions has been reported. Two important experiments, each with greater mass fraction sensitivity than that of the present work, have also been subsequently conducted, one by the Florida State group in collaboration with Cookson at the Harwell 3 MeV proton microprobe facility[21] and one by an Oak Ridge group at the synchrotron radiation facility at Stanford.[16] These are the only other experiments which have made use of giant halo inclusions and neither of these support a superheavy element interpretation of the anomalies reported herein.

The imponderables of spatial inhomogeneity and differential volatility have not been resolved to date. Work on a higher energy proton microprobe which can hopefully answer some of the open questions is in progress. The work with the present limited system has demonstrated that some weak but statistically significant transitions do not have a clear interpretation in terms of expected behavior of known x rays and γ rays. Although they could be explained by the presence of $L\alpha$ transitions from superheavy elements, the present data do not provide us with compelling evidence for previously unknown x-ray transitions. The search for superheavy elements in natural selected monazite samples, although many investigations are not encouraging at present, must proceed because of the extreme importance of definitive results.

---

*On leave from Department of Physics, University of California, Davis, California 95616.
[1]R. V. Gentry, Annu. Rev. Nucl. Sci. 23, 347 (1973).
[2]R. V. Gentry, T. A. Cahill, N. R. Fletcher, H. C. Kaufmann, L. R. Medsker, J. W. Nelson, and R. G.

Flocchini, Phys. Rev. Lett. 37, 11 (1976).
[3]S. A. E. Johansson and T. B. Johansson, Nucl. Instrum. Methods 142, 307 (1977).
[4]T. A. Carlson, C. W. Nestor, F. B. Malik, and T. C. Tucker, Nucl. Phys. A135, 57 (1969); C. C. Lu, F. B.

Malik, and T. A. Carlson, *ibid.* A175, 289 (1971).

[5]W. A. Deer, R. A. Howie, and J. Zussman, *Rock Forming Minerals* (Wiley, New York, 1962), Vol. 5, p. 342.

[6]B. Jensen and J. W. Nelson, Nucl. Instrum. Methods 93, 137 (1971).

[7]B. Jensen and J. W. Nelson, Nucl. Instrum. Methods 68, 284 (1969).

[8]H. C. Kaufmann, R. Akselsson, and W. Courtney, Nucl. Instrum. Methods 142, 251 (1977).

[9]J. Harrison and R. A. Eldred, Adv. X-ray Anal. 17, 560 (1974).

[10]D. C. Camp, A. L. Van Lehn, J. R. Rhodes, and A. H. Pradzynski, X-ray Spectrom. 4, 123 (1975); Florida State is coded in this reference as group No. 13.

[11]B. R. Doe, *Lead Isotopes* (Spring-Verlag, Berlin, 1970).

[12]R. K. Lyrick and T. A. Cahill, Phys. Rev. A 8, 2288 (1973).

[13]J. D. Fox, W. J. Courtney, K. W. Kemper, A. H. Lumpkin, N. R. Fletcher, and L. R. Medsker, Phys. Rev. Lett. 37, 629 (1976); N. R. Fletcher and J. D. Fox, Annual Report, Florida State University Tandem Accelerator Laboratory, Tallahassee, Florida, 1976 (unpublished), p. 68.

[14]F. Bosch, A. El Goresy, W. Krätschmer, B. Martin, B. Povh, R. Nobiling, K. Traxel, and D. Schwalm, Phys. Rev. Lett. 37, 1515 (1976); D. Schwalm, (private communication).

[15]N. R. Fletcher, Phys. Rev. Lett. 38, 479 (1977).

[16]S. Raman, Bull. Am. Phys. Soc. 22, 71 (1971); C. J. Sparks, Jr., S. Raman, H. L. Yakel, R. V. Gentry, M. O. Krause, Phys. Rev. Lett. 38, 205 (1977); and (unpublished).

[17]F. Petrovich, R. J. Philpott, D. Robson, J. J. Bevelacqua, M. Golin, and D. Stanley, Phys. Rev. Lett. 37, 558 (1976); C. Y. Wong, *ibid.* 37, 664 (1976); P. Moller and J. R. Nix, *ibid.* 37, 1461 (1976); G. Anderson, S. E. Larsson, G. Leander, S. G. Nilsson, I. Ragnarsson and S. Aberg, Phys. Lett. 65B, 209 (1976); M. Vallières and D. W. L. Sprung, *ibid.* 67B, 253 (1977).

[18]D. N. Schramm, W. A. Fowler, J. B. Blake, and K. L. Haineboch (unpublished).

[19]H. Schultheis and R. Schultheis, Phys. Rev. C 15, 1601 (1977); Phys. Lett. 49B, 423 (1974); 58B, 384 (1975).

[20]U. von Wimmersperg and J. P. F. Sellschop, Phys. Rev. Lett. 38, 886 (1977).

[21]J. A. Cookson, N. R. Fletcher, K. W. Kemper, L. Medsker, and T. A. Cahill, Annual Report, Florida State University Tandem Accelerator Laboratory, Tallahassee, Florida, 1976 (unpublished) p. 73; J. A. Cookson *et. al.* (unpublished).